

SMASIS2021-68209

COMPUTATIONAL AND EXPERIMENTAL EFFICIENCY INVESTIGATION OF NONLINEAR ENERGY HARVESTING SYSTEMS BASED ON MONOSTABLE AND BISTABLE PIEZOELECTRIC BEAMS

G. C. Kardarakos
University of Patras
Patras, GR

D. Varelis
Hellenic Air Force
Academy
Athens, Greece

N. A. Chrysochoidis
Affiliation Here
University of Patras

N. Margelis
National Technical
University of Athens
Athens, Greece

N. Leventakis
National Technical
University of Athens
Athens, Greece

T. S. Plagianakos
National Technical
University of Athens
Athens, Greece

G. Bolanakis
National Technical
University of Athens
Athens, Greece

D. A. Saravanos
University of Patras
Patras, Greece

E. Papadopoulos
National Technical
University of Athens
Athens, Greece

ABSTRACT

Piezoelectric energy harvesting from vibrating piezoelectric structures under nonlinear oscillations has been proved quite promising, with a large amount of scientific works focusing on the maximum energy harvested. However, the detailed dynamic response of an electromechanical coupled nonlinear vibrating system and the interaction between the piezoelectric structure and an external electric circuit deem to be an extremely important parameter of interpreting this complex dynamic phenomenon. The current work focuses on the development of a robust and accurate numerical tool capable of modelling such systems. This model aims to simulate the power dissipated at an external purely resistive circuit attached at a nonlinear oscillating piezoelectric beam subjected to different compressive loading. Experimental studies on a fabricated prototype are also conducted for different excitation frequencies and resistive loads, as to provide an estimation of the energy dissipated. In addition, a preliminary experimental study is performed to quantify the available electrical energy that is produced from the oscillating structure into three different harvesting circuits. Measured results exhibit their performance, indicate their benefits and drawbacks and at the end the most promising piezoelectric energy harvester is specified.

Keywords: piezoelectric, energy harvesting, geometric nonlinearity, non-linear vibration, finite element modelling, prebuckling, postbuckling

1. INTRODUCTION

Over the last decades, various research works have focused on the conversion of available energy from oscillating structures, into usable electric energy, providing an alternative power supply for low-power devices. One highly investigated approach to achieve this goal is via electromechanical energy conversion of piezoelectric composite strips and plates undergoing mechanical vibrations [1]. However, linear vibrations of such configurations have produced small amounts of harvested energy, thus current research attention is focused upon nonlinear piezoelectric energy harvesters (PEH) based on buckled (monostable and bistable) configurations of strips and plates [2]-[3]. Operating in the geometrical nonlinear regime these piezoelectric structures yield a broadband frequency response [4]-[5] and may thus be efficient in low frequency excitation ranges.

The PEH capability of nonlinear mechanisms has been initially studied in cantilever beams, equipped with piezoelectric transducers, subjected to magnetic forces [6]-[7]. Concerning oscillating beams subjected to compression, the effect of axial preload on natural frequency of a doubly hinged piezoelectric bimorph was studied by Leland and Wright [8]. Masana and

Daqaq extended the Galerkin formulation of Emam and Nayfeh [9] to beams with piezoelectric transducers [10] and studied the effects of excitation frequency, base acceleration and axial load on the power output to resistive circuits [11]-[12]. Simplified lumped-parameter (LP) models, were developed by Harne [13] and Cottone et al. [14]. Ansari and Karami developed a PEH device based on controlled buckling of a steel sheet with piezoelectric layers or patches, capable of producing power in the order of mWatts from passing car traffic [15]. A buckled spring-mass architecture was designed by Liu et al. and impedance matching technics were evaluated for maximizing output power [16]. Recently, Speciale et al. developed designed, manufactured and tested a double curved snap-through buckling mechanism connected to a rectifier and a capacitor [17].

In the works referenced above, resistive circuits were studied, focusing on proper tuning of the shunting resistance for maximum power extraction. However, PEH circuits applicable to IoT devices consist of charging and discharging subcircuits involving additional capacitors, switches and control, which affect the extracted power and overall performance of the harvesting device. Circuit design and power output optimization for linear PEH mechanisms have been thoroughly studied in the last two decades [18]-[25]. Huguet et al. reported 1.3–2.2 times higher power harvesting from a bistable PEH by designing an AC-DC electronic interface capable of synchronized electric charge extraction [26]. Wang et al. applied impedance modeling to nonlinear electric circuits and studied their interaction with a monostable beam using the harmonic balance method [27].

The current paper aims at presenting an electrical power production study of axially compressed composite beams under dynamic base excitation combining comprehensive reduced-order numerical FE models and experimental verification. The main objectives and contributions of the current study are trifold: the first is to develop a robust numerical tool based on a reduced-order piezoelectric plate finite element, capable to describe the power produced due to nonlinear vibrations at the terminals of piezo-devices attached on buckled strips; the second is to characterize, using a specially designed prototype configuration, the nonlinear vibrations of a compressed strip and the resultant electrical power production of a surface attached piezoelectric film on a resistive circuit; and the third to investigate the optimal energy harvesting from the oscillating structure using appropriate rectification circuits.

2. THEORETICAL FRAMEWORK AND NUMERICAL MODELING

In the current section, the piezoelectric laminate mechanics and the reduced-order plate finite element are introduced. The piezoelectric structure is assumed to undergo large-rotations in a Lagrangian framework, whereas the material of each ply or piezoelectric layer is assumed to follow the constitutive equations of linear piezoelectricity,

$$\begin{aligned} \sigma_i &= C_{ij}^{E,T} S_j - e_{ik}^T E_k & i, j &= 1, \dots, 6 \\ D_l &= e_{ij}^T S_j + \varepsilon_{lk}^{S,T} E_k & k, l &= 1, \dots, 3 \end{aligned} \quad (1)$$

where σ_i , S_j are the mechanical Piola-Kirchhoff stresses and Green's engineering strains in extended vectorial notation respectively, C_{ij} is the elastic stiffness tensor, e_{ik} is the piezoelectric tensor, E_k is the electric field vector, D_l is the electric displacement vector and ε_{lk} is the electric permittivity tensor. Superscripts E, S, T represent constant voltage, strain, and temperature conditions, respectively.

Kinematic Assumptions

The nonlinear multi-field piezoelectric laminate theory is adopted, which combines first shear deformation assumptions for the displacement field with a linear layerwise electric potential field, as a means of describing the kinematic assumptions of the state variables [30]-[31]. Furthermore, the theory takes large laminate rotations into account, according to the Von-Karman nonlinearity assumptions. Thus, the equivalent Green-Lagrange strains take the following form:

$$\begin{aligned} S_1 &= u_{,x}^o + z\beta_{x,x} + \frac{1}{2}w_{,x}^{o^2} \\ S_2 &= v_{,y}^o + z\beta_{y,y} + \frac{1}{2}w_{,y}^{o^2} \\ S_6 &= u_{,y}^o + v_{,x}^o + z(\beta_{x,y} + \beta_{y,x}) + w_{,x}^o w_{,y}^o \\ S_4 &= w_{,y}^o + \beta_y \\ S_5 &= w_{,x}^o + \beta_x \end{aligned} \quad (2)$$

where u^o , v^o are the midplane in-plane displacements along the x and y directions, respectively, while w^o is the transverse displacement; β_x and β_y are the bending rotation angles about the y and x axes, respectively. The three last RHS terms of the S_i strains ($i=1,2,6$) express the nonlinear strain components S_{Li} respectively, with all referred to the mid-surface A_o . The subscript “,” denotes spatial derivative in respect to the axis following the subscript.

The approximation of electric fields within a piezoelectric layer which is located between the thickness points z_{m+1} and z_m is provided by the following expressions:

$$\begin{aligned} E_1(x, y, z) &= -(\Phi_{,x}^{m+1}(x, y)\Psi^{m+1}(z) + \Phi_{,x}^m(x, y)\Psi^m(z)) \\ E_2(x, y, z) &= -(\Phi_{,y}^{m+1}(x, y)\Psi^{m+1}(z) + \Phi_{,y}^m(x, y)\Psi^m(z)) \\ E_3(x, y, z) &= -(\Phi^{m+1}(x, y) - \Phi^m(x, y))/h_m \end{aligned} \quad (3)$$

where $h_m = z_{m+1} - z_m$ is the thickness of the layer; Φ^{m+1} and Φ^m indicate the electric potentials at the corresponding thickness points, and Ψ^m are interpolation functions through the thickness of the piezoelectric laminate.

Generalized Dynamic Equations of Motion in Variational Form

Based on the principle of Virtual Work and neglecting the physical damping of the piezoelectric structure, the equations of

motion of the piezoelectric laminate plate, mandate that the work of generalized imbalances between external and internal multifield forces Ψ_u and electric charges Ψ_e , should vanish at equilibrium, at any time t over the volume V of the piezoelectric laminated plate [32].

$$\begin{aligned} \delta^t u^T {}^t \Psi_u &= \int_V \delta^t S^T {}^t \sigma dV + \int_V \delta^t u^T \rho^t \ddot{u} dV \\ &\quad - \int_V \delta^t u^T {}^t b dV - \int_{\Gamma_\tau} \delta^t u^T {}^t \bar{\tau} d\Gamma = 0 \quad \text{at equilibrium} \end{aligned} \quad (4)$$

$$\delta^t \varphi^T {}^t \Psi_e = \int_V \delta^t E^T {}^t D dV - \int_{\Gamma_q} \delta^t \varphi^T {}^t \bar{q} d\Gamma = 0 \quad \text{at equilibrium}$$

where ${}^t b$, $\rho^t \ddot{u}$ denote body and inertia body forces respectively, ${}^t \bar{\tau}$, ${}^t \bar{q}$ are the surface tractions and electrical charge applied on the boundary surface Γ_τ and piezoelectric terminal boundary surface Γ_q , respectively. Left superscript t indicates the time step, and overdot represents the time derivative.

Coupled nonlinear plate finite element

An eight-node coupled plate finite element, integrating the previous coupled mechanics is implemented, which approximates the electromechanical state variables on the reference mid-plane A_o with local interpolation functions [32].

Discrete Dynamic Equations of Motion

Substituting the FE approximation into Eqs. (4) and assuming no actuators on the structure, the following coupled system of nonlinear discrete equations of motion is derived for time step t , indicated as upper left symbol:

$$\begin{aligned} {}^t \Psi_u(u, \varphi) &= [M] {}^t \ddot{u} + [{}^t K_{uu}(u)] {}^t u + [{}^t K_{ue}(u)] {}^t \varphi^f - (5) \\ {}^t F_b - {}^t F &= 0 \\ {}^t \Psi_e(u, \varphi) &= [{}^t K_{eu}(u)] {}^t u + [{}^t K_{ee}] {}^t \varphi^f - {}^t Q^f = 0 \end{aligned}$$

where, $u = \{u, v, w, \beta_x, \beta_y\}^T$ is the nodal displacement vector, φ^f is the free nodal electric potential at the piezoelectric elements. K_{uu} is the effective stiffness matrix, K_{ue} is the inverse piezoelectric matrix, K_{eu} is direct piezoelectric matrix, all of which include linear and nonlinear terms and K_{ee} is the effective electric permittivity matrix which includes only linear terms. ${}^t F_b$ and ${}^t F$ are the body and external force vectors, used for the base acceleration excitation and the axial compressive load respectively; and ${}^t Q^f$ is the electric charge extracted from the piezoelectric element into an external electric circuit.

It is noted that the stiffness and piezoelectric matrices in the previous equations contain linear and nonlinear components related to the initial stresses and the large transverse deflections “ w ”, which may result in nonlinear monostable and bistable vibrations. In the following Eqs. the linear and nonlinear

(dependence on u) components of the K_{uu} , K_{ue} , K_{eu} , K_{ee} matrices are displayed related to the large transverse deflections, while the initial stress effect is shown in the end of the current subsection.

$$\begin{aligned} [K_{uu}(u)] &= [K_{uu}^o] + [K_{uu}^L] = [K_{uu}^o] + [P_1(u)]/2 + [P_2(u^2)]/3 \\ [K_{ue}(u)] &= [K_{ue}^o] + [K_{ue}^L] = [K_{ue}^o] + [P_3(u)] \\ [K_{eu}(u)] &= [K_{eu}^o] + [K_{eu}^L] = [K_{eu}^o] + [P_4(u)]/2 \\ [K_{ee}] &= [K_{ee}^o] \end{aligned} \quad (6)$$

Contrary to the simplified assumptions of previously reported lumped modes, it is evident that the large rotations in a vibrating buckled beam does not only provide membrane stiffening, but also affect the piezoelectric charge terms, and the piezoelectric coupling. The linear and nonlinear components of the above-described matrices have been analytically presented in refs. [31],[33].

When an external purely resistive electric circuit is attached to the piezoelectric material terminals, the expression that correlates the electric potential with the charge flow is presented below:

$${}^t \varphi^f = [R] {}^t \dot{Q}^f \quad (7)$$

where ${}^t \dot{Q}^f$ indicates the electric current or the electric charge flow generated at the external resistive load and $[R]$ expresses the discretized resistive load at the nodes where the piezoelectric material and the external circuit are connected.

Combining the Eq. (5) with the nonlinear discrete equations of motion, the final discrete dynamic set of equations is formed:

$$\begin{aligned} \begin{bmatrix} [M] & 0 \\ 0 & 0 \end{bmatrix} {}^t \begin{Bmatrix} \ddot{u} \\ \dot{Q}^f \end{Bmatrix} + \begin{bmatrix} 0 & 0 \\ 0 & [R] \end{bmatrix} {}^t \begin{Bmatrix} \dot{u} \\ \dot{Q}^f \end{Bmatrix} + \\ \begin{bmatrix} [K_{uu}] - [K_{ue}][K_{ee}]^{-1}[K_{eu}] & [K_{ue}][K_{ee}]^{-1} \\ [K_{ee}]^{-1}[K_{eu}] & -[K_{ee}]^{-1} \end{bmatrix} {}^t \begin{Bmatrix} u \\ Q^f \end{Bmatrix} = \begin{Bmatrix} {}^t F_{TOT} \\ 0 \end{Bmatrix} \end{aligned} \quad (8)$$

where ${}^t F_{TOT} = {}^t F_b + {}^t F$.

It is noted that the final equations of motion have been manipulated, such that free DoFs contain the mechanical displacements $\{u\}$ and the extracted electric charge vector $\{Q^f\}$. Thus, the electric charge extracted from the piezostructure to the external electric circuit can be directly computed.

Moreover, one could also observe that as the mechanical damping of the system is neglected, the energy of the vibrating structure is dissipated only in the resistive load. Hence, the external resistive load plays a dual role, as it defines the amount of the energy extracted and dissipated to the electric circuit and provides damping to the piezoelectric structure.

Solution Scheme for Discretized Coupled Nonlinear Equations of Motion

The solution schemes adopted for solving the coupled nonlinear equations of motion are briefly mentioned. At first, an axial compressive displacement is applied at one end of the piezoelectric composite beam, while the other end remains fixed. This loading stage could be characterized as pseudo-static, as no dynamic loading is exerted in the structure. The method utilized for solving the nonlinear equations is the Displacement Control method, and assuming also that the solution point cannot be directly achieved, the Newton-Raphson iterative technique is implemented to linearize the coupled nonlinear equations at each iteration.

After the end of prestressing, the dynamic loading begins when the piezoelectric composite beam is exerted under a dynamic excitation. In this regard, the trapezoidal rule of Newmark's time integration method is adopted for solving the final discrete coupled nonlinear dynamic system at each time step, along with the Newton-Raphson technique. Thus, the tangential matrices which compose the final linearized system of equations are described below:

$$\begin{aligned} [\bar{K}_{uu}(u)] &= \frac{4}{\Delta t^2} [M] + [\bar{K}_{uu}^o] + [\bar{K}_{uu}^\sigma] + [\bar{P}_1(u)] + [\bar{P}_2(u^2)] \\ [\bar{K}_{ue}(u)] &= [\bar{K}_{ue}^o] + [\bar{K}_{ue}^L] = [\bar{K}_{ue}^o] + [\bar{P}_3(u)] \\ [\bar{K}_{eu}(u)] &= [\bar{K}_{eu}^o] + [\bar{K}_{eu}^L] = [\bar{K}_{eu}^o] + [\bar{P}_4(u)] \\ [\bar{K}_{ee}] &= [\bar{K}_{ee}^o] \end{aligned} \quad (9)$$

where the stress stiffness matrix \bar{K}_{uu}^σ includes the effect of initial linear mechanical and piezoelectric stresses in the tangential stiffness matrix.

Detailed information about the steps for each method have been described in previous scientific works [31],[33] for corresponding open-circuit problems.

3. EXPERIMENTAL CONFIGURATION

The experimental configuration includes the electromechanical subsystem, comprising of an axially loaded composite beam with a centrally attached piezoelectric patch subjected to base excitation, and the electrical subsystem, including charging and output circuits. Each subsystem is described separately in the following.

Electromechanical Subsystem

A special experimental setup was built to enable dynamic tests on axially loaded composite beams. The experimental setup is illustrated in Figure 1. The setup consists of a horizontal platform made of aluminum, which is capable to oscillate laterally on a pair of horizontal slides. A pair of vertical steel supports are mounted on the base. On the right vertical corner (see Figure 1) there is the mount where the specimen is placed

directly. On the other end the vertical steel corner block is mounted on micrometer stage, providing accurate application of horizontal displacement to the specimen. Additionally, the left mount is also equipped with a static canister load cell capable of measuring the axially generated force due to horizontal compression of the specimen from the mechanism. Finally, the left mount of the specimen is directly and rigidly mounted on the load cell. Using the current setup, the specimen is mounted under clamped-clamped boundary conditions. The whole setup is oscillated laterally via an electromechanical shaker mounted on the horizontal platform with simply intervening a dynamic load cell to record the applied force from the shaker to the specimen. During the experiment, the resulting acceleration of the platform and the specimen are continuously acquired.

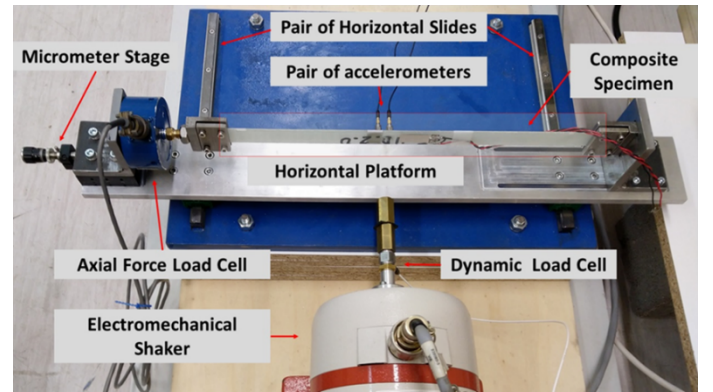


Figure 1: Experimental setup.

Electrical Subsystem

Three types of PEH circuits have been studied (Figure 2): i) in-house (cc-ih), ii) custom, using off-the-shelf commercial hardware (cc-ch) and iii) commercial, designated as E-821.00 by PI (cc-PI) [28]. The in-house harvesting circuit (cc-ih), consists of a diode rectifier due to the alternating input current, a capacitor which charges accumulating electric current and a load with a switch which discharges the capacitor in a controlled manner to a battery. The custom commercial PEH circuit (cc-ch), includes an SPV1050 energy harvester [29], modified to include a rectification stage, a STEVAL-ISV020V1 evaluation board and a battery charger. This harvester implements maximum power point tracking (MPPT) and integrates the switching elements of a buck-boost converter. The commercial circuit E-821.00 manufactured by PI (cc-ch) is an integrated circuit that includes a diode rectifier and a capacitor that charges up to 12V, activating then an automatic switch which allows part of the electrical energy in the capacitor to be released into a secondary sub-circuit. The automatic switch is turned off when the voltage of the capacitor falls at 6V. The switch is implemented by a MOSFET controlled by an operational amplifier which compares the voltage of the capacitor to a reference voltage. The secondary circuit consists of a buck converter and voltage clipper that assures that the output is a pulse of constant voltage.

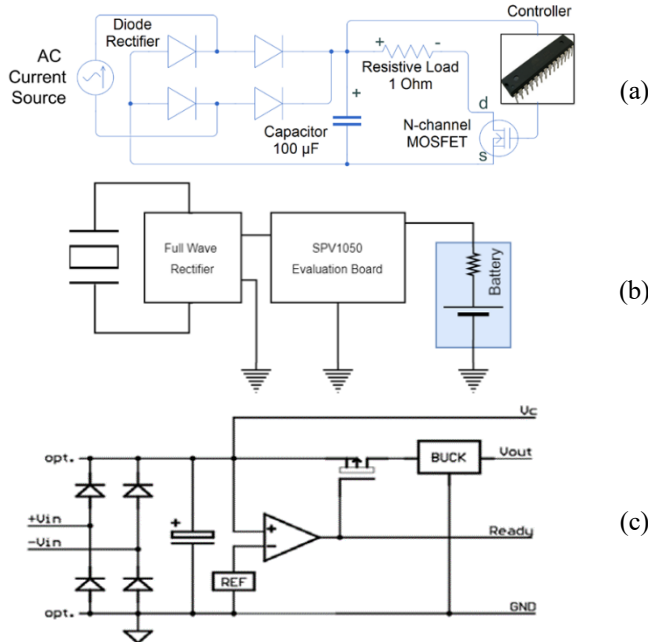


Figure 2: PEH circuits: (a) cc-ih, (b) cc-ch, (c) cc-PI.

4. RESULTS AND DISCUSSION

A composite beam with a centrally placed DuraAct [P-876.A12] piezoelectric transducer [34] and a concentrated 5g mass is studied in various loading levels covering the full range of pre- and post-buckling loading range. The results include experimental validation in open circuit, resistive circuits and measurements performed with resistive and PEH circuits.

Materials

The material of the beam is Glass/Epoxy with mechanical properties listed in Table 1.

Table 1 Material properties.

Property	Composite	Piezoelectric	Polyimide
Density (kg/m^3)	1672	7800	1420
<i>Elastic Properties</i>			
E_{11} (GPa)	25.766	62.34	2.5
E_{22} (GPa)	8.746	62.34	2.5
E_{33} (GPa)	8.746	52.44	2.5
G_{12} (GPa)	3.527	23.02	0.933
G_{13} (GPa)	3.527	21.29	0.933
G_{23} (GPa)	2.362	21.29	0.933
ν_{12}	0.344	0.354	0.34
ν_{13}	0.344	0.464	0.34
ν_{23}	0.4675	0.464	0.34
<i>Piezoelectric Properties</i>			
d_{31} (10^{-12} m/V)	-	-190.9	-
d_{32} (10^{-12} m/V)	-	-190.9	-
d_{33} (10^{-12} m/V)	-	-	-
<i>Dielectric Properties</i> ($\epsilon^0=8.85 \cdot 10^{-12}$ F/m, strain-charge)			
ϵ_{33}/ϵ^0	3.01	1534	0.384

The beam dimensions are $349 \times 24.75 \times 1.3 \text{ mm}^3$. A 0.2 mm thick DuraAct piezoelectric patch from PI, considered to be enclosed in two Kapton/Polyimide layers of 0.15 mm thickness each, was adhesively bonded on the beam. The properties considered for the piezoceramic and polyimide materials are also included in the following Table.

Open-circuit response

In this subsection, the experimental study focuses on the investigation of the small-amplitude (linearized) vibration of the beam subject to axial loads when no external electric circuit is connected to piezoelectric material. The developed numerical tool was used to design the experiment, and conversely it was correlated with the measurements from the described experiments.

During the experimental procedure the specimen was axially loaded by applying displacement via the left mounted micrometer stage (see Figure 1). The loading was interrupted in steps of axially generated force on the static load cell and a modal testing was performed on the specimen with small levels of lateral mechanism excitation via the electromechanical shaker. The actuation signal was a white-noise in the range 0 to 200 Hz and during the actuation the acceleration was acquired by the pair of accelerometers to provide the net specimen acceleration. FRFs were extracted using the net specimen acceleration and the measured force through the dynamic load cell. Fitting the FRFs with a numerical tool based on complex and exponential terms the modal frequency of the specimen's 1st bending mode was extracted. Similar simulations were performed using the numerical tool. The correlation between the numerical simulation and the experimental measurements was performed for the variation of the small-amplitude fundamental modal frequency of the beam and is shown in Figure 3. In the matter of the numerical simulations, the FE mesh density was 20×1 elements for all cases investigated.

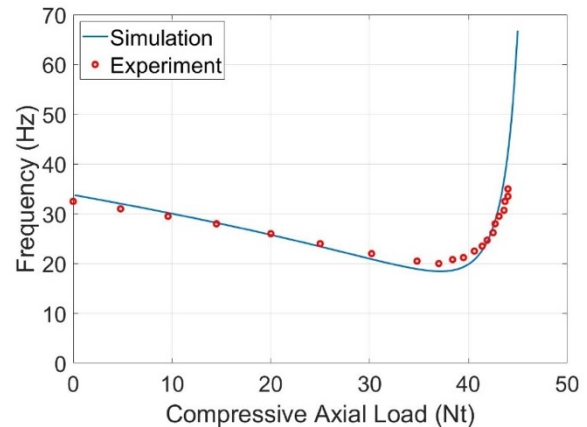


Figure 3: Small amplitude vibration response of the piezoelectric composite beam under axial compressive force.

Very good agreement between the experimental and simulated results, all over the range of the axial prestress loading, was obtained. This correlation reveals that the piezoelectric

composite beam approaches quite well the ideal response of a beam with infinitesimal initial imperfections. Regarding the critical buckling load, where the 1st bending mode reaches its minimum value, it was found experimentally and numerically to be at 37 Nt.

Resistive circuits

In this case the variation of the produced power is investigated as a function of the applied axial compressive force. The RMS voltage was measured at the terminals of the resistance and the produced power was calculated. Aiming to maximize the extracted power production, the optimal resistance for each excitation frequency, corresponding to the case of linear vibration under no-axial load, was connected on the piezoelectric patch terminals. Base oscillation was performed in three frequencies 5 Hz, 8 Hz and 18 Hz all of them smaller than the beam modal frequencies as presented in Figure 3. During the experimental procedure, the beam was axially loaded, interrupting the loading procedure at various load steps, and performing lateral dynamic excitation. Figure 4 (a) and (b) demonstrate the variation of the measured power as a function of the applied axial load for two base acceleration levels 1g and 2g.

It is obvious that as the axial load increases and the structure stiffness decreases, the power production rises exponentially. However, it seems that there exists a limit point, which bounds this exponential increase. Specifically, the beam undergoes monostable vibrations in the prebuckling regime, which may turn to bistable vibrations in the postbuckling regime. Hence, in the postbuckling regime, the specimen can oscillate in two different ways: to perform intrawell oscillations vibrating around one of the two stable equilibrium attractors, resulting in lower amplitude oscillations; or to perform interwell oscillations of larger amplitude, where the specimen transitions from one stable state attractor to another. If there is not enough energy to enable the interwell oscillation, then the specimen's deflections are significantly decreased resulting to the reductions of the power shown in Figure 4, in the postbuckling range.

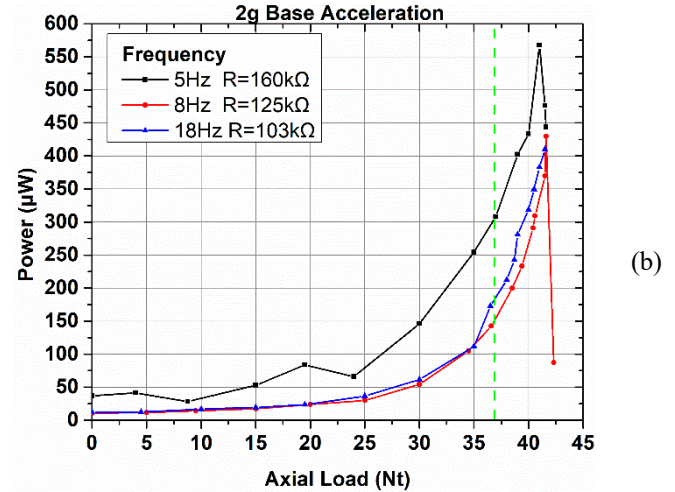
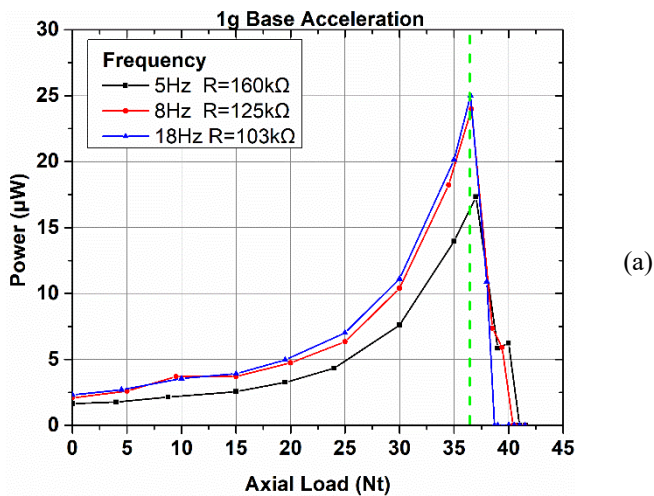


Figure 4: Variation of the resistance power as a function of the applied axial load for (a) 1g and (b) 2g base acceleration.

As mentioned above in case the base acceleration is set at 1g a drastic reduction at the measured power is recorded for lower levels of prestress compared to 2g base acceleration, due to earlier initiation of the intrawell oscillation. On the other hand, if interwell oscillations occur, power production remains high.

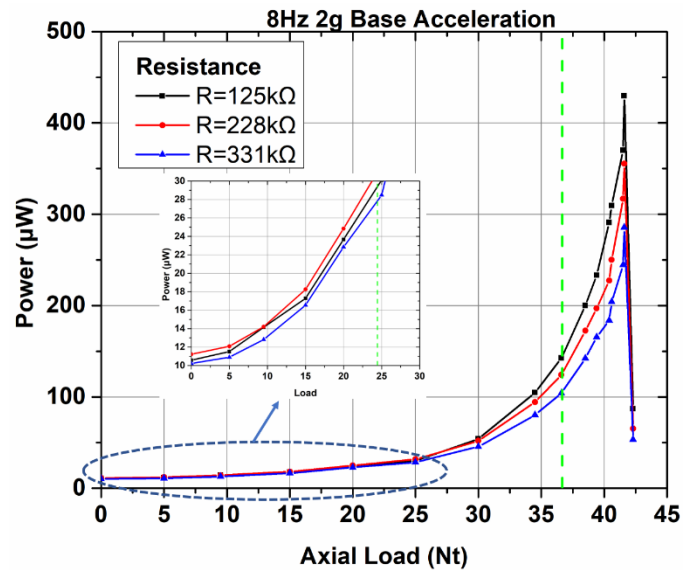


Figure 5: Effect of shunting resistance as a function of the applied compressive load.

Additionally, the resistance tuning is demonstrated for 8 Hz and 2g base acceleration in Figure 5. Three different resistance levels were connected: an $R_2 = 228 \text{ k}\Omega$ resistance that yields the maximum power harvesting for the case of linear vibrations under zero axial pre-stress, one smaller ($R_1 = 125 \text{ k}\Omega$) and one

larger ($R_3=331 \text{ k}\Omega$). Initially, the higher production is achieved for the R_2 resistance. However, this trend seems to change as the axial load approaches the critical buckling load, where the maximum power is provided by the small resistance. This is a critical observation indicating the need to adapt the impedance of the harvesting circuit that requires further investigation.

The numerical tool predictions are shown in interpreting Figure 6 for the case of 8 Hz excitation frequency and 1g base acceleration level for the external resistive $R_2 = 228 \text{ k}\Omega$.

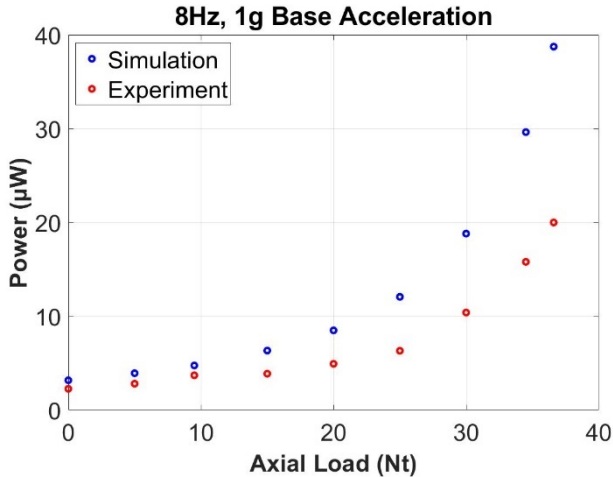


Figure 6: Predicted and measured variation of the resistance power as a function of the applied axial load, for 8 Hz and 1g base acceleration.

It is obvious in Figure 6, that there exists reasonable agreement between the numerical model and the experimental results. The former overestimates the generated power as the level of prestress increases, a fact that was expected since the physical damping of the specimen was not considered in the model. Previous studies [35] have demonstrated very high sensitivity of the viscoelastic material damping of composite beams to the prestress load and buckling state, that follows opposite trend to the modal frequency shown in Figure 3. Consequently, a comprehensive investigation of the damping effect and modeling should be conducted in the upcoming future along with a more appropriate discretization of the resistive load, all of which could significantly affect the harvested electric power.

PEH circuits

In the latter study case, the power extracted from the vibrating piezoelectric structure to the PEH circuits, is examined. Three different types of PEH were tested, each of which provide an estimate of the power that could be exploited from the system. Based on the conclusion of the previous section relative to increased power production in case the structure is loaded to postbuckling regime we focus current study under this state. So the composite beam is subjected under 43 Nt axial load and at this state the structure modal frequency is measured at 32.5 Hz (see Figure 3).

Initially, circuits performance was studied at 5 and 8 Hz frequency excitation. Figure 7 illustrates the time response of voltage at charging circuit capacitor and output current in cc-ih circuit for a 2g base acceleration. It is interesting that within a small frequency range (5 – 8 Hz) the PEH circuit seems to charge two times slower.

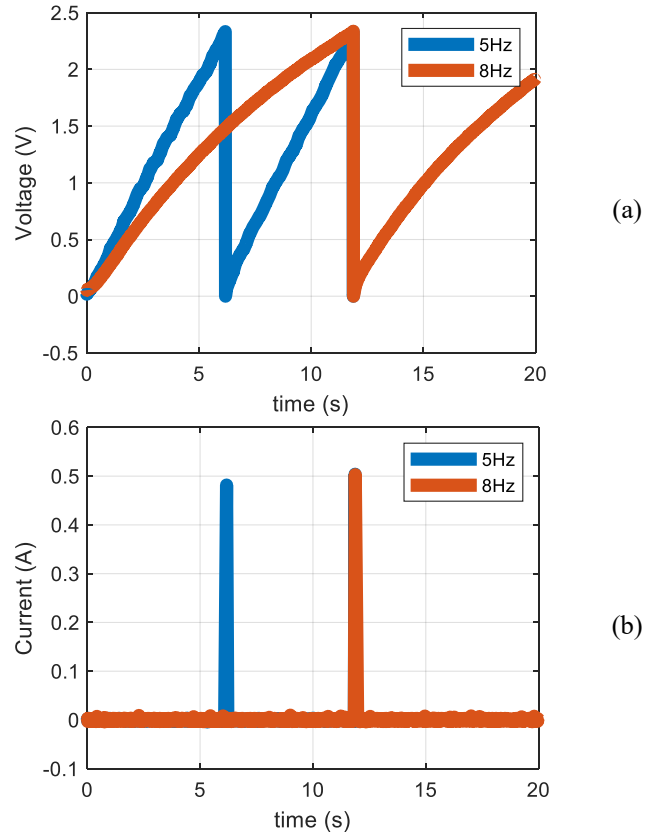


Figure 7: Effect of frequency on time response in cc-ih at 2g base acceleration: (a) $V_c(t)$, (b) $I_{out}(t)$.

The voltage and current time signals at the battery connected to the output subcircuit of the other two PEH circuits, cc-ch and cc-PI, are shown in Figure 8 and Figure 9, respectively, at 2g base acceleration in the low frequency range. As in the case of the cc-ih, both circuits harvest more power at 5 Hz. This trend is smoother in the case of the cc-ch, probably due to the impedance matching function of the circuit. In the case of cc-PI, effects of noise may be also observed, especially in electric current signals, which are related to the connection of the PEH module with the data acquisition terminal board. The different timescale between these two circuits is also noted, as it indicates the capability of the cc-ch to provide power output more often.

The effect of base acceleration on the harvested power in cc-ih and cc-ch circuits at “resonance” 32.5 Hz is shown in Figure 10. The measurements in both circuits indicate that there is no continuous increase in power with base acceleration. It is interesting that cc-ch harvests at maximum for maximum base acceleration in the studied range, but practically not at all at 0.5g. Modeling of the coupled electromechanical closed-circuit

response is expected to contribute to clear up these trends and lead to proper tuning.

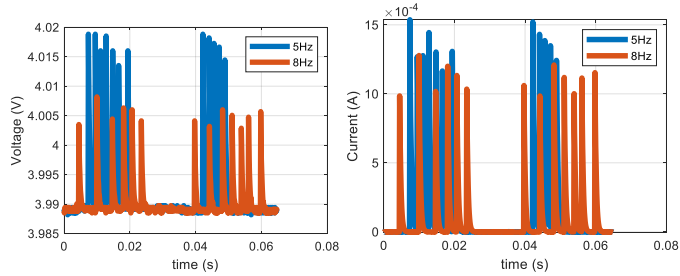


Figure 8: Effect of frequency on time response in cc-ch at 2g base acceleration: left: $V_{bat}(t)$, right: $I_{bat}(t)$.

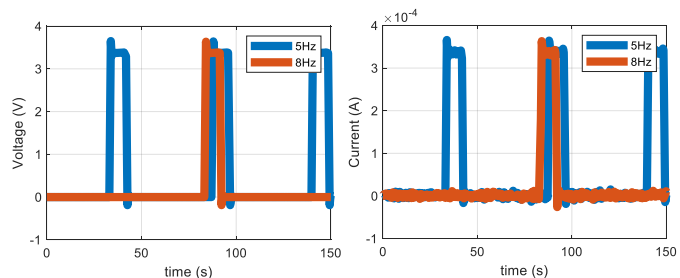


Figure 9: Effect of frequency on time response in cc-PI at 2g base acceleration: left: $V_{bat}(t)$, right: $I_{bat}(t)$.

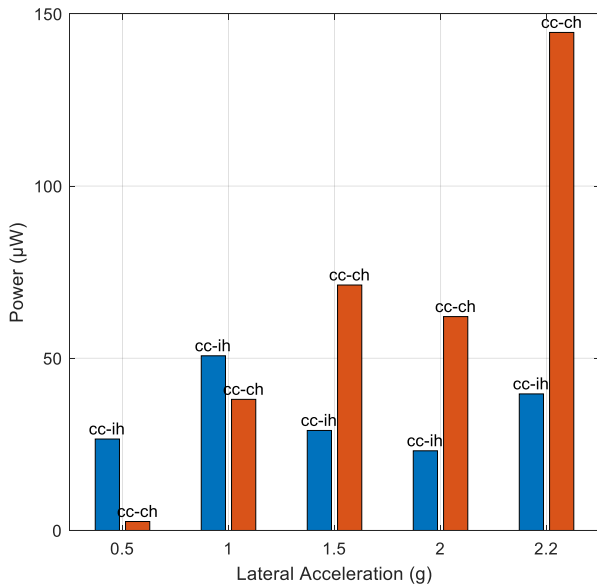


Figure 10: Effect of base acceleration on electric power output at 32.5Hz.

A comparative study between the three PEH in terms of power output at 2g base acceleration and low frequencies is presented in Figure 11. Clearly, at 5 Hz more power is harvested in all circuits and a similar comparative trend is observed. The cc-ch is the most productive circuit in the studied range. It is also

very important to mention that comparing the harvested power of this circuit versus the measured produced power at the resistance terminals (cc-R), the efficiency of this circuit varies between 56% and 40% for operation at 5 Hz and 8 Hz respectively. This remarkable performance indicates the importance of impedance matching between the piezoelectric and the harvesting circuit. On the other hand, the low harvested power from the cc-ih highlights the sensitivity of harvested power to circuit losses at the μW harvesting range, as achieved experimentally.

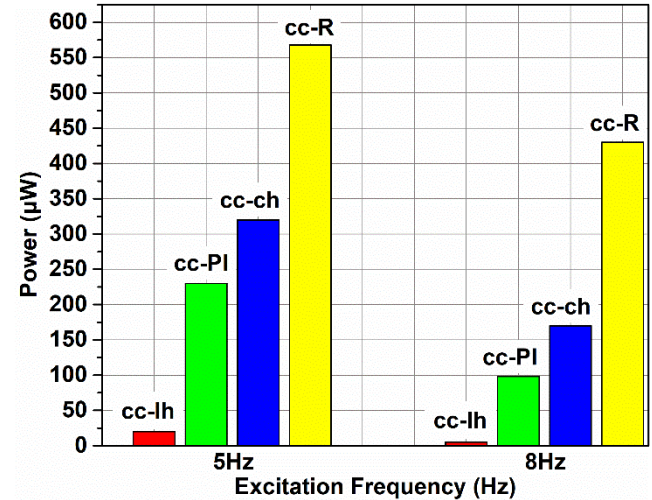


Figure 11: Output electric power at 5 Hz and 8 Hz excitation frequency and 2g acceleration were cc-R refers to the power produced on the resistance.

5. CONCLUSION AND FUTURE WORK

A combined experimental and computational campaign was conducted to analyze and quantify various factors affecting the efficiency of energy harvesting in vibrating nonlinear piezoelectric-composite strips subject compressive loading. In the computational front, an efficient numerical nonlinear structural dynamics framework was expanded to simulate the attachment of an external resistive circuit on piezoelectric vibrating beams. The aim of the modelling was to predict the power dissipated at the resistive load, in order to provide the basis of the interaction between the electromechanical subsystem and the electric circuit. Obtained preliminary numerical results have provided good correlations with the experimental results. In the experimental campaign, experimental studies were conducted on prestressed composite strips with DuraAct piezoelectric patch considering a purely resistive circuit connected at the piezoelectric material terminals.

The obtained results presented indicated that the axial prestress level has a major contribution at the power dissipated. In addition, the maximum power dissipation occurs when the beam vibrates in the postbuckling regime and adequate energy exists to enable interwell oscillations. Concerning the optimal resistive load that could dissipate the maximum power, it was found that this changes, as the prestress load reaches the critical

buckling load, and further investigation is required to be conducted in the future to shed light on this observation.

Finally, three different types of PEH were examined for the power that could harvest. The PEH circuits were tested at the postbuckling regime and the outcome was that the most promising PEH circuit was found to be the custom commercial PEH circuit (cc-ch) due to its impedance matching capability. It was finally computed that for 5 Hz excitation frequency its efficiency exceeds the 50%.

ACKNOWLEDGEMENTS

This research has been co-financed by the European Regional Development Fund of the European Union and Greek national funds through the Operational Program Competitiveness, Entrepreneurship and Innovation, under the call RESEARCH – CREATE – INNOVATE (project code: T1EDK-01533).

REFERENCES

- [1] Safaei M, Sodano HA, Anton SR. *A review on energy harvesting using piezoelectric materials: state-of-the-art a decade later (2008-2018)*. Smart Materials and Structures, 28(11), 1-63, 2019.
- [2] Harne RL, Wang, KW. *A review of the recent research on vibration energy harvesting via bistable systems*. Smart Materials and Structures 22, 023001, 2013.
- [3] Jia Y. *Review of nonlinear vibration energy harvesting: Duffing, bistability, parametric, stochastic and others*. Journal of Intelligent Material Systems and Structures 31(27), 921-944, 2020.
- [4] Cette P, Sneller AJ, Mann BP. Investigations of natural frequencies and vibration mode shapes for a post-buckled beam with different attached masses. Proceedings of the ASME DSCC conference, DSCC2010-425.
- [5] Jung SM, Yun KS. *A wideband harvesting energy device using snap-through buckling for mechanical frequency-up conversion*. 2010 IEE 23rd International Conference on MEMS.
- [6] Wickenheiser AM, Garcia E. *Broadband vibration-based energy harvesting improvement through frequency up-conversion by magnetic excitation*. Smart Materials and Structures 19(6), 065020, 2010.
- [7] Erturk A, Inman DJ. *Broadband piezoelectric power generation on high-energy orbits of the bistable Duffing oscillator with electromechanical coupling*. Journal of Sound and Vibration 330(10), 2339-2353, 2011.
- [8] Leland ES, Wright PK. *Resonance tuning of piezoelectric vibration energy scavenging generators using compressive axial preload*. Smart Materials and Structures 15(5), 1413-1420, 2006.
- [9] Emam SA, Nayfeh AH. *On the nonlinear dynamics of a buckled beam subjected to a primary-resonance excitation*. Nonlinear Dynamics 35, 1-17, 2004.
- [10] Masana R, Daqaq MF. *Electromechanical modeling and nonlinear analysis of axially loaded energy harvesters*. Journal of Vibration and Acoustics 133(1), 011007, 2011.
- [11] Masana R, Daqaq MF. *Relative performance of a vibratory energy harvester in mono- and bi-stable potentials*. Journal of Sound and Vibration 330, 6036-6052, 2011.
- [12] Masana R, Daqaq MF. *Energy harvesting in the superharmonic frequency region of a twin-well oscillator*. Journal of Applied Physics 111(4), 044501, 2012.
- [13] Harne R. *Theoretical investigations of energy harvesting efficiency from structural vibrations using piezoelectric and electromagnetic oscillators*. Journal of the Acoustical Society of America 132(1), 162-172, 2012.
- [14] Cottone F, Gammaitoni L, Vocca H, Ferrari H, Ferrari V. *Piezoelectric buckled beams for random vibration energy harvesting*. Smart Materials and Structures 21(3), 035021, 2012.
- [15] Ansari MH, Karami MA. *Energy harvesting from controlled buckling of piezoelectric beams*. Smart Materials and Structures 24, 115005, 2015.
- [16] Liu WQ, Badel A, Formosa F, Wu YP, Agbossou A. *Novel piezoelectric bistable oscillator architecture for wideband vibration energy harvesting*. Smart Materials and Structures 22, 035013, 2013.
- [17] Speciale A, Ardito R, Bau M, Ferrari M, Ferrari F, Frangi AA. *Snap-through buckling mechanism for frequency-up conversion in piezoelectric energy harvesting*. Applied Sciences 10, 3614, 2020.
- [18] Ottman GK, Hoffmann HF, Bhatt AC, Lesieutre GA. *Adaptive piezoelectric energy harvesting circuit for wireless remote power supply*. IEEE Transactions on Power Electronics 17(5), 669-676, 2002.
- [19] Lefeuvre E, Badel A, Richard C, Guyomar D. *Piezoelectric energy harvesting device optimization by synchronous electric charge excitation*. Journal of Intelligent Material Systems and Structures 16, 865-876, 2005.
- [20] Lefeuvre, E, Audigier D, Richard C, Guyomar D. *Buck-boost converter for sensorless power optimization of piezoelectric energy harvester*. IEEE Transactions on Power Electronics, 22(5), 2018-2025, 2007.
- [21] Lallart M, Garbuio L, Petit L, Richard C, Guyomar D. *Double synchronized switch harvesting (DSSH): a new harvesting scheme for efficient energy extraction*. IEEE Transactions on Ultrasonics, Ferroelectrics, and Frequency Control, 55(10), 2119-2130, 2008.
- [22] Shen H, Qiu J, Ji H, Zhu K, Balsi M. *Enhanced synchronized switch harvesting: a new energy harvesting scheme for efficient energy extraction*. Smart Materials and Structures 19(11), 1-14, 2010.
- [23] Liang J, Liao WH. *Impedance modeling and analysis for piezoelectric energy harvesting systems*. IEEE/ASME Transactions on Mechatronics 17(6), 1145-1157, 2012.
- [24] Ramadass YK, Chandrakasan AP. *An efficient piezoelectric energy harvesting interface circuit using a bias-flip rectifier and shared inductor*. IEEE Journal of Solid-State Circuits 45(1), 189-204, 2010.
- [25] Tabesh A, Frechette LG. *A low-power stand-alone adaptive circuit for harvesting energy from a piezoelectric*

micropower generator. IEEE Transactions on Industrial Electronics 57(3), 840-849, 2010.

[26] Huguet T, Lallart M, Badel A. *Bistable vibration energy harvester and SECE circuit exploring their mutual influence*. Nonlinear Dynamics 97(5), 485-501, 2019.

[27] Wang J, Zhao B, Liao WH, Liang J. *New insight into piezoelectric energy harvesting with mechanical and electrical nonlinearities*. Smart Materials and Structures 29(4), 04LT01, 2020.

[28] E-821 Electronic module for energy harvesting using piezo actuators for energy generation. PI Motion/Positioning, 2014.

[29] Datasheet SPV1050 Ultralow power energy harvester and battery charger. STMicroelectronics, 2018.

[30] Varelis D, and Saravanos DA. *Mechanics and finite element for nonlinear response of active laminated piezoelectric plates*. AIAA Journal 42(6), 1227-1235, 2004.

[31] Varelis D, Kardarakos G-C, Chrysochoidis N and Saravanos DA. *Towards a nonlinear buckled piezoelectric*

beam system for enhanced electromechanical energy conversion. Proc. SPIE 11376, 1-17, 2020.

[32] Varelis D, and Saravanos DA. *Coupled finite element for the nonlinear dynamic response of active piezoelectric plates under thermoelectromechanical loads*. J. Mech. Mater. Struct. 4(7), 1489-1503, 2009

[33] Kardarakos GC, Chrysochoidis NA, Varelis D, Saravanos DA, Plagianakos TS, Vartholomeos P, Leventakis N, Bolanakis G, Margelis N, Papadopoulos EG. *Piezoelectric energy harvesting from composite beams in geometric nonlinear regime: numerical and experimental approach*. Proc. SPIE 11588, 1-17, 2021.

[34] <https://www.piceramic.com/en/products/piezoceramic-actuators/patch-transducers/p-876-duraact-patch-transducer-101790/>

[35] Chortis DI, Varelis DS, and Saravanos DA. *Linearized frequencies and damping in composite laminated beams subject to buckling*. Journal of Vibration and Acoustics 135(2), 1-10, 2013